doi:10.20944/preprints202203.0321.v1

Article

Optimal Design of an Interior Permanent Magnet Synchronous Motor with Cobalt Iron Core

Pedro P. C. Bhagubai[1], Luís F. D. Bucho[1], João F. P. Fernandes[1*] and P. J. Costa Branco[1]

[1.] IDMEC, Instituto Superior Técnico, University of Lisboa, Lisboa, Portugal
pedro.bhagubai@tecnico.ulisboa.pt, luis.bucho@tecnico.ulisboa.pt, joao.f.p.fernandes@tecnico.ulisboa.pt, pbranco@tecnico.ulisboa.pt,
* Correspondence: joao.f.p.fernandes@tecnico.ulisboa.pt

† This is an extension of the conference paper: P. P. C. Bhagubai, A. C. Cardoso and J. F. P. Fernandes, "Cobalt Iron Core Impact on Optimal Design of an Interior Permanent Magnet Synchronous Motor for Competition Electric Vehicle," 2020 2nd Global Power, Energy and Communication Conference (GPECOM), 2020, pp. 158-163.

Abstract: The use of cobalt-iron (VaCoFe) core is investigated as an alternative to silicon-iron (FeSi) on the design of interior permanent magnet synchronous motors (IPMSM). A spoke-type IPMSM geometry is optimized considering FeSi and VaCoFe cores for a torque range up to 40 N.m, providing a general comparative analysis between materials, considering the application of a 4-motor competition vehicle's powertrain. A genetic optimization algorithm is applied over a hybrid analytical/finite-element model of the motor to provide sufficiently accurate electromagnetic and thermal results within a feasible time. VaCoFe can result in an estimated increase of up to 5 % in efficiency for the same torque, or up to 64 % torque increase for the same efficiency level. After optimization, and using a detailed time-dependent model, a potential 3.2 % increase in efficiency, a core weight reduction of 4.1 %, and a decrease of 9.6 % in the motor's core volume was found for the VaCoFe at 20 Nm. In addition, for the same motor volume, the VaCoFe allows an increase of 51.9 % of torque with an increase of 1.1 % of efficiency, when compared with FeSi.

Keywords: electric vehicle; electromagnetic model; optimization; silicon-iron; thermal model; Vanadium Cobalt

1. Introduction

Higher power density and efficiency in electrical machines is a constant pursuit among research and industrial communities. These characteristics lead to lighter, higher efficiency machines, which are extremely advantageous in applications with limited energy storage, such as electric mobility and transportation. In this sense, the development of electrical machines has been made by a combined approach of applying new magnetic materials and by optimizing their topologies. This is a particular important issue in the development of all-electric aircrafts, where the required target of 9-13kW/kg still remains to be achieved [1].

The Vanadium-Cobalt-Iron (VaCoFe) alloy has been emerging as a potential candidate to increase the current electrical machines' limits on power density and efficiency, as it is characterized by a high saturation point (2.2-2.4T) [2]. However, due to higher magnetic densities, this may lead to a higher contribution of losses, making it unclear whether the reduced core volume achieved with VaCoFe is enough to maintain a high efficiency, when compared to classic FeSi cores, for the same power. The thermal limit aspect also becomes relevant as high core losses may prevent full use of VaCoFe's high magnetic flux density. So far, several studies have identified the potential of using VaCoFe to increase the specific-power of electrical machines in Synchronous Reluctance Machines [3-5] and Permanent Magnet Synchronous Machines [6-7], for high-speed and aerospace applications. In electric car traction applications, few have successfully applied

VaCoFe comparatively to FeSi, with some reports stating an increase of at least 20% in specific torque/power concerning FeSi machines [8-9]. Also, an important target in aircraft applications is increasing the current limits of electrical machines (around 5kW/kg) to values of 9-13kW/kg for future electric aircraft applications [10]. In [6] the use of VaCoFe has shown the possibility of increasing specific power up to 10kW/kg and increasing the efficiency by about 3% in aircraft applications.

In [11], a high-performance spoke-type IPMSM to be integrated into a 4-motor vehicle powertrain has been designed with a FeSi core. The designed motor was built and validated through experimental tests. To improve the performance of this vehicle, VaCoFe is considered as a promising material, and, as such, a question arises on quantifying the influence of the core material on machine design and performance. A spoke-type IPMSM geometry is optimized considering FeSi and VaCoFe cores for a range of torque/efficiency to provide a general comparative analysis between materials for the application. The non-dominated sorting genetic algorithm II (NSGA-II) [12] is used over a hybrid analytical/finite-element (FE) model of the motor, similar to the method validated before [11]. This kind of electrical machine design based on optimization tools using hybrid analytical/FE models is a successful method [13] that also takes less computation time than purely FE models [14] while providing good results. It allows large-scale design optimization to achieve high-power density designs of permanent magnet-based machines as IPMSM [15] and other topologies such as novel axial flux PMSM [16]. Particularly in [15], large scale multi-objective optimization using a differential evolution algorithm with a FE model was applied to obtain an optimal spoke-type IPMSM design for a Formula E competition (110 N.m at 6000 rpm), experimentally validated, achieving 12.2 N.m/kg. Additionally, obtaining optimal designs allows a comparative analysis between motor characteristics, such as winding configuration or cooling system, as was done in [17] for a 300 N.m, 1800 rpm IPMSM machine. In this work, the focus is on the core lamination material.

Our presented motor model provides sufficiently accurate electromagnetic and thermal results and can be computed within a feasible time in the context of the optimization process. It consists of a stationary time 2D FE model used to calculate the motor’s flux distribution, in conjunction with analytical expressions to estimate losses in the core and permanent magnets and the operating temperature. From these, the parameters of the IPMSM equivalent circuit are computed, and torque and efficiency values are obtained. Each core material is characterized by its B-H and power loss density constitutive curves. Because the optimization results are highly dependent on the accuracy of the model, experimental BH and specific loss curves are obtained for a test magnetic circuit of VaCoFe laminations.

Based on this model, we show in this work that VaCoFe core results in higher torque and efficiency across the considered ranges, with an estimated increase of up to 5% in efficiency for the same torque, or up to 64% torque increase for the same efficiency level. However, because the density of VaCoFe is higher than FeSi, and because it is possible to have larger PMs and slots in VaCoFe designs, there is a less pronounced difference in weight for the overlapping torque range. Because VaCoFe laminations are around three times more expensive than FeSi due to its material cost and post-processing requirements to achieve optimal proprieties [2], whether the difference in specific torque and the increase in efficiency achieved with VaCoFe concerning FeSi cores is considerable enough to justify these increased costs has to be subject to further application-specific cost/benefit analysis.

This work follows the preliminary work developed in [18], by including new experimental tests to the VaCoFe alloy and its impact on the optimization. A more detailed analysis of the optimized solutions, using a time-dependent FE approach, is carried to obtain accurate results for torque ripple, harmonics, and losses. A 4-motor competition electric vehicle’s powertrain, with 80 N.m at 8000 rpm, is here considered as a case-study.

2. Electric motor materials

This study focuses on the impact of different magnetic core materials in the IPMSM's performance, in particular, using FeSi and VaCoFe. For the IPMSM modeling and optimization, these are characterized by their respective B-H and specific losses curves with a density of 7650 kg/m3 for FeSi and 8120 kg/m3 for VaCoFe.

The B-H curve of VaCoFe is estimated from experimental tests on a sample magnetic circuit. The test circuit is made of two 'E'-type lamination stacks, with two windings around the central leg, Figure 1. A sinusoidal voltage is applied on the primary winding with various amplitudes, enough to saturate the circuit. For each applied voltage, the current in the primary winding and induced voltage in the secondary winding are measured to estimate the peak magnetic field intensity, H, and flux density, B, Figure 2 .The VaCoFe laminations are estimated to reach a BH curve knee-point around 2.0T. The specific losses curve is presented for a frequency of 400Hz, which is the nominal frequency of the machine, and additionally for 50Hz for a reference. This material's properties have been shown to be sensitive to the manufacturing process, however if an appropriate cutting followed by heat treatment process is applied to the laminations it is possible to limit the negative impact, and reach values up to 2.4T [2]. The tested circuit's laminations were treated according to the manufacturer's specifications and, as such, specific losses are close to the predicted properties, presented in the datasheet, for both frequencies, Figure 3. However, there is still a more noticeable deviation around the knee-point for the BH curve results, which were considered in the optimization process.

A high-performance, low losses FeSi alloy for electrical machines is considered, with a BH curve knee-point around 1.5T. It has been characterized for optimization previously in [11] with the prototyping of a 20kW FeSi PMSM, and the results are presented for comparison, Figure 2 and Figure 3.

For both cases, NH40 grade Neodymium-Boron (NdFeB) permanent magnets are considered with remnant magnetic flux B_r=1.2T. The shaft is made of stainless steel, a non-magnetic material.

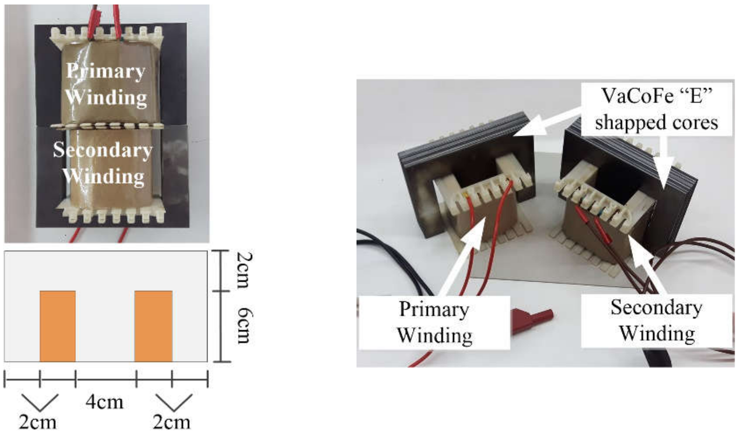

(**a**) (**b**)

Figure 1. Magnetic circuit made from VaCoFe used in the experimental tests. (a) Magnetic circuit dimensions and (b) Core and windings' identification.

doi:10.20944/preprints202203.0321.v1

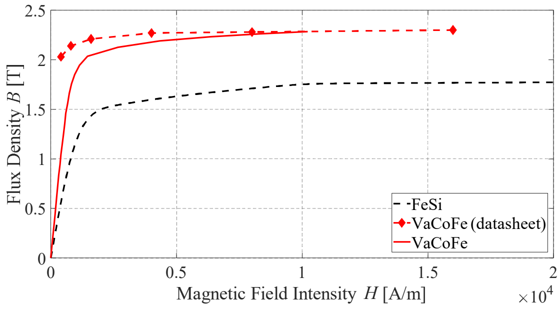

Figure 2. B-H curve of lamination materials: FeSi, VaCoFe obtained experimentally and from manufacturer’s datasheet.

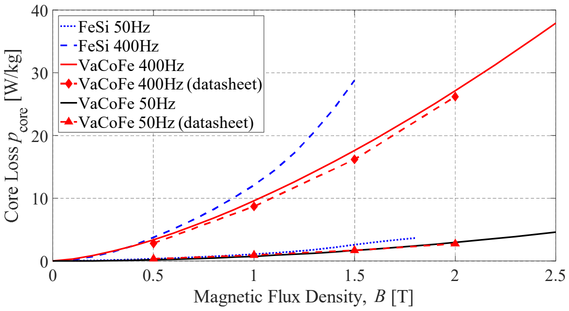

Figure 3. Specific losses curve of lamination materials: FeSi, VaCoFe obtained experimentally and from manufacturer’s datasheet, at 50Hz and 400Hz.

3. Spoke-type interior permanent magnet synchronous machine model

The presented model considers the electromagnetic and thermal aspects of the IPMSM and it is based on a FE model used to compute lumped parameters of analytical expressions. This type of model is chosen for computationally intensive optimizations because it provides a compromise between computation time and accuracy [14]. To maintain a low computation time, the geometry of the core is simplified and only a pole pair of the machine is modeled. A stationary time 2D FE model is used to calculate the motor’s flux distribution and, in conjunction with analytical expressions, operating temperatures, efficiency, and torque are estimated.

This methodology is used for the multi-objective optimization of the machine. After optimization, the final solutions are simulated using a time-dependent study. The proposed model was validated experimentally for a similar geometry of IPMSM, with the FeSi core considered in Figure 2. This FeSi IPMSM was previously developed and experimentally tested in [11]. In this previous work, the same electromagnetic-mechanical models were used (2D FE model + analytical models) to simulate a IPMSM with FeSi for a 4-motor competition electric vehicle’s powertrain that was required to develop a total maximum of 80 N.m at 8000 rpm to achieve the desired performance. An example of a competition track with an optimized lap is presented in Figure 4 along with the total torque profile in Figure 5. After simulation and verification of the fulfillment of the requirements, a final solution of the machine was built and tested. After some mechanical adjustments in the rotor, to facilitate the cutting of the laminated silicon iron, a rated torque and efficiency of 18.2 N.m and 90.0%, respectively. The machine was built and tested, Figure 6, and the efficiency map obtained from experimental tests, shown in Figure 7.

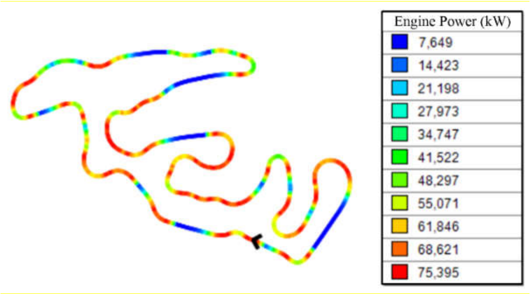

Figure 4. FSAE Autocross Germany track simulation.

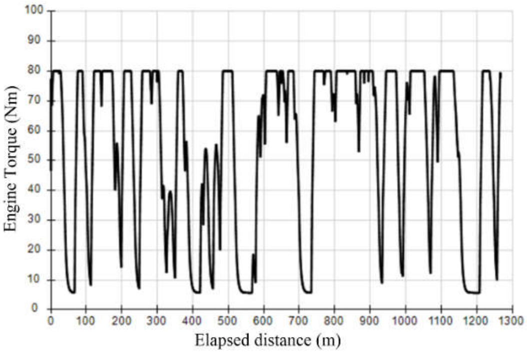

Figure 5. Instantaneous motor's torque along the track.

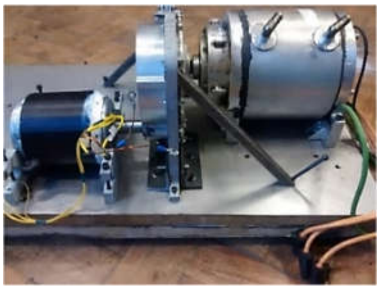

Figure 6. 20kW IPMSM with FeSi core in experimental setup [11].

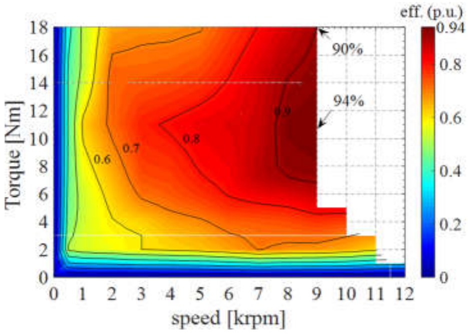

Figure 7. Torque-efficiency map obtained experimentally [11].

Following the previous work, a new IPMSM with VaCoFe is now optimized and compared with the results of an optimized FeSi machine. This is intended to evaluate the potential of extending the limits of the IPMSM using VaCoFe alloys.

3.1. Geometry and winding layout

Figure 8 shows the base geometry of the IPMSM to be optimized using FeSi and VaCoFe. This base geometry was developed and validated for a 20 kW 8000 rpm IPMSM in [11]. It has a 24-slot stator and an 8-pole rotor, with the variable dimension parameters shown in Figure 8 (rotor, r_r, and shaft radius, r_s, the permanent magnet width, w_m, and length, l_m, the stator tooth width, w_t and length, l_t, outer ring width, w_s, and the airgap size, g). These parameters will be decision variables in the optimization process to maximize the IPMSM's torque and efficiency.

The slot/pole combination is chosen according to the nominal rotation speed required for the competition vehicle. Because the competition car has four identical motors mounted in the suspension of each wheel, the outer dimensions are limited to the available space. The maximum outer radius and length are equal to 50 mm and 80 mm, respectively. In the stator, a single-layer concentrated winding layout was adopted to maximize the fundamental component of the airgap magnetomotive force wave and to simplify the manufacturing process (Figure 8).

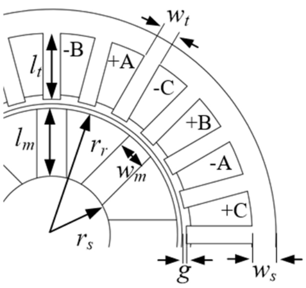

Figure 8. Interior permanent magnet synchronous machine model geometry and winding layout.

3.2. Electromagnetic model

The optimization is an iterative process requiring a high number of simulations, which can result in very high computational times. To reduce the computational optimization time to a feasible time, a hybrid analytical/finite element (FE) model was used to represent the IPMSM. The analytical model is based on the synchronous *d-q* reference frame IPMSM equivalent circuit, considering iron losses, Figure 9. To obtain the machine's equivalent circuit parameters, a 2D stationary FE model is used. Using the FE model, the magnetic flux linkages, the machine's *d-q* inductances, L_d and L_q, and the equivalent core-loss resistance, R_c, are estimated.

The steady-state torque, which has two components: the electromagnetic, T_{EM}, and reluctance torque, T_{Rel}; can be computed using (1), where n_{pp} is the number of pole pairs, Ψ_{PM} is the permanent magnet linked flux and i_{od}, i_{oq} are the torque generating currents. The torque generating currents, i_{od}, i_{oq}, are calculated using the IPMSM's *d-q* equivalent circuits, in Figure 9, after obtaining the machine's parameters with the FE model. In Figure 9, v_d, v_q, i_d, i_q are the *d-q* axis stator voltages and currents, i_{od}, i_{oq} are the torque generating currents, R_s is the phase winding resistance, R_c is the equivalent core-loss resistance, L_d and L_q are the *d-q* inductances, ω_M is the rotor angular speed, and Ψ_{PM} the permanent magnet linked flux which, for the considered machine topology, is aligned with the *d*-axis.

$$T = T_{EM} + T_{Rel} = \frac{3}{2} n_{pp} \left(\Psi_{PM} i_{oq} + \left(L_d - L_q \right) i_{od} i_{oq} \right) \tag{1}$$

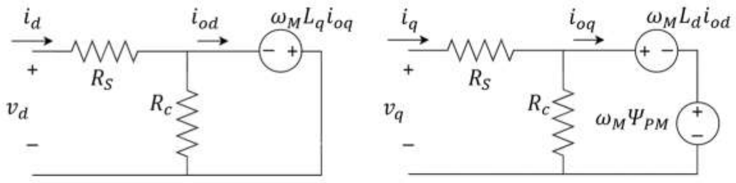

Figure 9. Synchronous machine equivalent circuit considering core-losses on a d-q reference frame.

The electromagnetic component of the generated torque was chosen to be optimized as it provides a good indication of the total torque of the machine, and it simplifies the machine's model equations, thus reducing its computational time. With $i_{od} = 0$, one obtains (2)-(4), which decreases the number of FE simulations required, as the computation of L_d is no longer required.

$$T = T_{EM} = \frac{3}{2} n_{pp} \Psi_{PM} i_{oq} \tag{2}$$

$$i_d = -\frac{\omega_M L_q i_{oq}}{R_c} \tag{3}$$

$$i_q = i_{oq} + \frac{\omega_M \Psi_{PM}}{R_c} \tag{4}$$

Losses estimation in the magnetic core and permanent magnets is traditionally made from time-dependent FE simulations for a certain rotation speed to include the effect of harmonics [19-20]. However, these have a high computational time and would make the genetic optimization process unfeasible. Therefore, analytical expressions for the locked-rotor case considering only the magnetic flux fundamental component are considered [21]. For optimization purposes, this rough estimation of iron losses is enough, and a more accurate loss model is applied later to some selected optimized motor designs to refine the obtained solutions further.

With these considerations, core loss density, p_{core}, is estimated with Steinmetz coefficients, obtained from the experimental results done and presented in Figure 2 and Figure 3, (5). Considering a sinusoidal variation of the flux density in the rotor and stator cores, where f is the frequency of the flux density and B_m is the amplitude of the flux density, the Steinmetz coefficients k_h, k_e and k_{exc} were determined for each core, VaCoFe and FeSi. The amplitude of flux density is obtained from the stationary FE model, with the stator flux aligned with d and q rotor axes.

$$p_{core} = k_h f B_m^2 + k_e (f B_m)^2 + k_{exc} (f B_m)^{1.5} \tag{5}$$

Losses density in permanent magnets, p_{PM}, are estimated from (6), which is an analytical approximation valid for parallelepiped shape magnets, not considering skin effect [22]. In (6), ρ_{PM}, d_{PM}, and l_{PM} are the resistivity, depth, and length of the permanent magnet, respectively. The magnets' length is the stack length (80mm). These losses could be minimized for the final design by segmenting the magnets, limiting induced current paths [22].

$$p_{PM} = \frac{(\pi f B_m)^2}{8 \rho_{PM}} \left(\frac{d_{PM}^2 l_{PM}^2}{d_{PM}^2 + l_{PM}^2} \right) \tag{6}$$

After the computation of the core and permanent magnets loss densities, the equivalent resistance R_c can be computed by (7), where V_{core} and V_{PM} are the rotor plus stator core volume and permanent magnets volume, respectively.

$$R_c = \frac{3}{2} \frac{\left(\omega_M (L_d i_{od} + \Psi_{PM})\right)^2 + \left(\omega_M L_q i_{oq}\right)^2}{p_{core} V_{core} + \rho_{PM} V_{PM}} \tag{7}$$

3.3. Finite element model

To reduce the complexity and computation time of the model, only one pole pair of the machine is simulated. To do this, a cut along flux density distribution symmetry lines with continuity conditions imposed on the boundaries is done, Figure 10. Each domain is defined as its corresponding materials: copper coils, magnetic core, NdFeB PMs, and stainless-steel shaft. Stationary-time simulations for the d-q axes are considered, and the current in each phase is given by (8). Depending on if the rotor's q (θ = 90°) or d (θ = 0°) axis is aligned with phase A, the Park transformation results in i_{od}=0 and i_{oq}=I_m or i_{od}=I_m and

i_{oq}=0, respectively. By adjusting the rotor's position, d-q linked fluxes Ψ_q and Ψ_d, and B_q and B_d flux density distributions can be estimated from FE model simulations.

$$\begin{aligned} i_A &= I_m cos(\omega t) \\ i_B &= I_m \cos(\omega t - 2\pi/3) \\ i_C &= I_m \cos(\omega t + 2\pi/3) \end{aligned} \tag{8}$$

With i_{od} = 0, Ψ_q and Ψ_{PM} are obtained from the stationary FE model. Without considering permanent magnets flux (Ψ_{PM} = 0), Ψ_q is obtained as a function of i_{oq} current, by aligning the rotor q-axis with the stator in a position of minimum flux linkage with stator coil (coil A). For simplification, cross saturation is neglected, and L_q is estimated as depending only on respective i_{oq}, (9). The permanent magnet linked flux, Ψ_{PM}, is obtained by aligning d-axis with stator coil A, with zero current (i_{od} = 0) and measuring the d-axis linked flux.

$$L_q = \left.\frac{\Psi_q}{i_{oq}}\right|_{i_{od}=0} \tag{9}$$

The estimation of R_c from locked-rotor core losses depends on the amplitude of flux density B_m in the PMs, rotor and stator (10). B_d and B_q are obtained by simulations with the stator flux aligned with d and q rotor axes and $\Psi_{PM} \neq 0$.

$$B_m = \left|B_d - B_q\right| \tag{10}$$

Flux distribution results are also used to evaluate magnetic saturation along with the core. The maximum magnetic flux density is evaluated along the strategic lines of the magnetic circuit (blue lines in Figure 10). In the rotor, the average flux density is computed, as the non-uniform flux distribution here makes it difficult to be characterized by a line. If the maximum flux density value in these lines or the average flux density in the rotor is above a defined threshold, the core is considered to violate the magnetic constraint. This method is used to avoid localized peaks of high flux concentration resulting in the rejection of promising geometries during optimization.

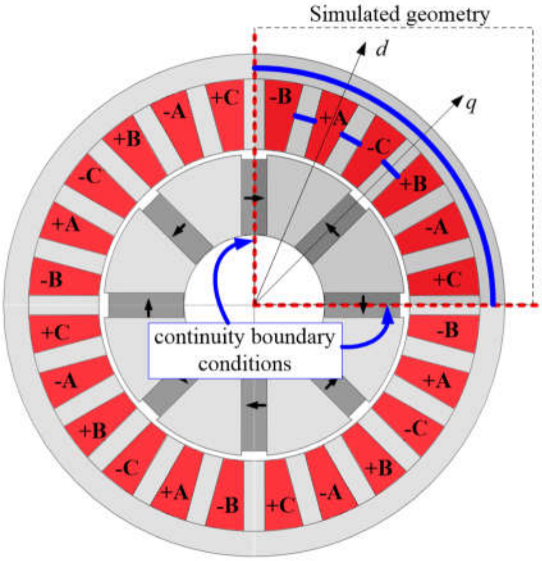

Figure 10. Finite Element Model of an example geometry representation with the rotor's q-axis aligned with phase A.

3.4. Maximum operating temperature estimation

Thermal phenomena in the machine are critical to determining if a design is viable or not. A simplified model was used to estimate the maximum operating temperature of the machine during optimization with low computational time. The motor will be required to provide nominal power in short bursts, so the maximum operating steady-state temperature can be estimated for the worst-case scenario to evaluate if the optimized solutions are viable. It will be water-cooled by a previously designed and implemented system that achieved a heat transfer coefficient of h = 1053 Wm^{-2}K^{-1} [11].

The estimation considers convective heat transfer in the airgap and dissipation from the machine surface to the cooling system and environment. Thermal conduction in the rotor and stator core are neglected as the conductive thermal resistance in metallic materials is very low when compared to the convective ones. The machine produces heat from Joule losses in the rotor core, (5), and PMs (6), which is dissipated through the airgap and, together with stator core and copper windings' losses (11), through the cooling jacket and into the environment.

$$P_{Cu} = \frac{3}{2} R_s\left(i_d^2 + i_q^2\right) \tag{11}$$

The airgap convective heat transfer coefficient is defined by (12) for heat transfer between concentric rotating cylinders(13)(14) [23]. In these, k is the air's thermal conductivity, D_h is the hydraulic diameter, Nu the Nusselt number, ν the air's kinematic viscosity, and ω_M the rotor's mechanical rotational speed. For the typical range of this motor's speed and the considered geometrical dimensions, Taylor's number Ta is greater than 10^4, and the flow will be turbulent; thus, Nu is given by (13).

$$h_{ag} = \frac{k}{D_h} Nu \tag{12}$$

$$Nu = 0.409\, Ta^{0.241} \tag{13}$$

$$Ta = \frac{{\omega_M}^2 (r_r + g)\left(\frac{D_h}{2}\right)^3}{\nu^2}, D_h = \frac{2\left(\pi\left((r_r + g)^2 - r_r^2\right)\right)}{\pi\left((r_r + g) - r_r\right)} \tag{14}$$

The convection thermal resistances of the airgap, R_{ag}, and of the machine's surface to the environment through the cooling system, R_S are obtained from (15) and (16). In these, $S_{ag} = 2\pi r_r L$ is the airgap heat transfer surface and $S = 2\pi RL$ is the electric machine's surface with outer radius R and length L. The heat transfer is described by the thermal equation system (17), where T_s and T_{amb} are the surface and ambient temperatures.

$$R_{ag} = \frac{1}{h_{ag} S_{ag}} \tag{15}$$

$$R_S = \frac{1}{hS} \tag{16}$$

$$\begin{cases} T_s = R_S(P_{stator} + P_{Cu}) + T_{amb} \\ T_{rotor} = R_{ag}(P_{rotor} + P_{PM}) + T_s \end{cases} \tag{17}$$

4. Optimization

The optimization is made to obtain the highest torque and efficiency values, with the machine dimensions subjected to the available space in the vehicle and the thermal safety limitations. The objectives functions defined in (18) are the maximizations of the electromagnetic torque (19) and efficiency (20) at 400Hz. This is a multi-objective optimization; therefore, optimized results are represented by a 2D curve (torque *vs.* efficiency). To perform the machine's optimization, the multi-objective genetic algorithm NSGA-II [12] is used, combining the results from the FE and analytical models. The NSGA-II is resilient to local optimal points, making it suitable for finding the global minimum/maximum of the solution space, populating it evenly, which is relevant for the intended comparative analysis.

$$\max_{x\in\Omega}\left(f_1(x), f_2(x)\right) \tag{18}$$

$$f_1 = T_{EM} = \frac{3}{2} n_{pp} \Psi_{PM} i_{oq} \tag{19}$$

$$f_2 = \eta = \frac{T_{EM}\omega_M}{T_{EM}\omega_M + p_{core}V_{core} + \rho_{PM}V_{PM}} \tag{20}$$

Geometrical decision variables are presented in Figure 8, which will be optimized within the ranges listed in Table 1. In addition to these, the torque producing current density, J_{oq}, is also optimized to account for temperature constraints. A winding slot filling factor of f_w=0.4 is considered.

Table 1. Optimization decision variables.

Variable	Description	Range
r_r	Rotor radius	20–40 mm
w_s	Stator outer ring width	1–20 mm
w_m	Magnet width	1–15 mm
l_m	Magnet length	5–20 mm
w_t	Teeth width	1–10 mm
l_t	Teeth length	7–20 mm
g	Airgap size	1–1.5 mm
r_s	Shaft radius	5–30 mm
J_{oq}	Torque producing current density (q axis)	5–80 A/mm^2

Constraints are listed in Table 2. These include constraints derived from application-specific requirements, such as maximum dimensions and weight, but also thermal limitations of windings and permanent magnets, and maximum magnetic flux density. The latter is set as 1.6T for FeSi and 2.2T for VaCoFe. Objective functions and constraints are evaluated with the presented electromagnetic and thermal models for each element of each generation.

Table 2. Optimization constraints by type and respective ranges.

Type	Constraint	Range
Geometrical	Weight	<5kg
	Stator outer radius	<50mm
	Motor stack length	=80mm
Thermal	PM's temperature	<120ºC
	Windings' temperature	<180ºC
Magnetic	Magnetic flux density	FeSi: <1.6T VaCoFe: <2.2T

5. Results

One optimization was made for each material, FeSi and VaCoFe magnetic cores. Each genetic optimization was done for 150 generations with 200 population elements each, which was enough for the solutions to converge within a feasible time (26 hours for FeSi and 30 hours for VaCoFe). The Pareto front curves, with objective function values from the last generation, are presented in Figure 11 and Figure 12. In terms of the objectives, VaCoFe core results in higher torque and efficiency values. It is estimated that VaCoFe can increase up to 5% in efficiency for the same torque (23N.m) or increase torque up to 64% for the same efficiency level (93.3%). It is noted that this increase is due to the relatively flat profile of the efficiency curve obtained for optimization, so it is highly dependent on its estimation according to the presented model. The accuracy of the model was validated previously for a 20kW FeSi PMSM built and tested in [11], and experimentally obtained curves are considered here for the VaCoFe core.

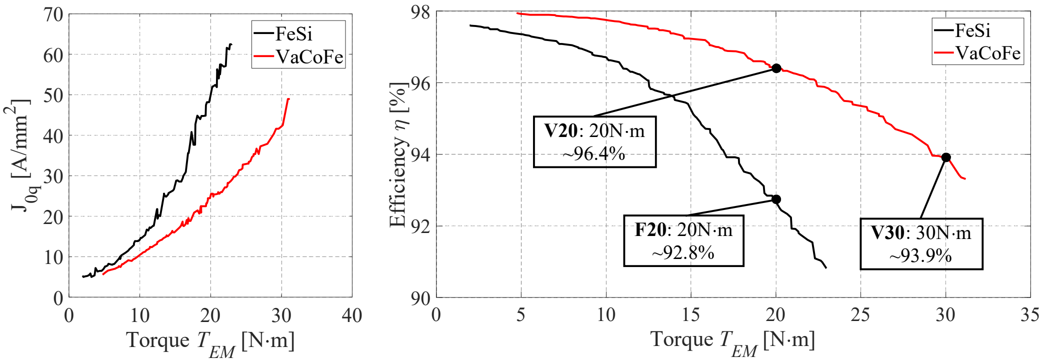

(**a**) (**b**)

Figure 11. Decision variable for FeSi and VaCoFe core optimization sorted by increasing torque: a) torque producing current density J_{oq} and b) Pareto front with objective functions efficiency and electromagnetic torque values of the last generation. Geometries selected for further analysis are represented.

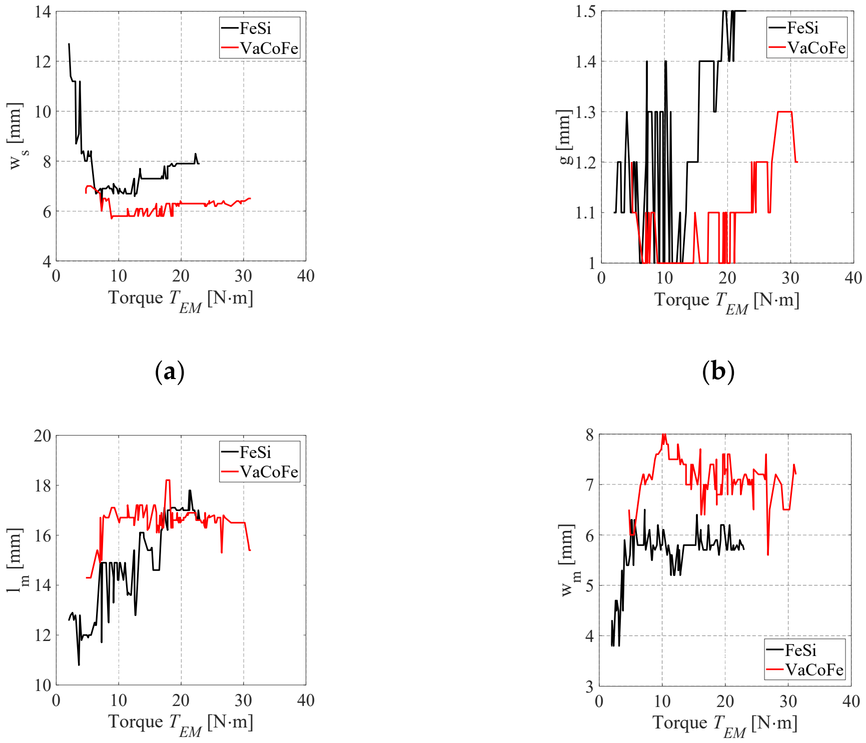

(**a**) (**b**)

(**c**) (**d**)

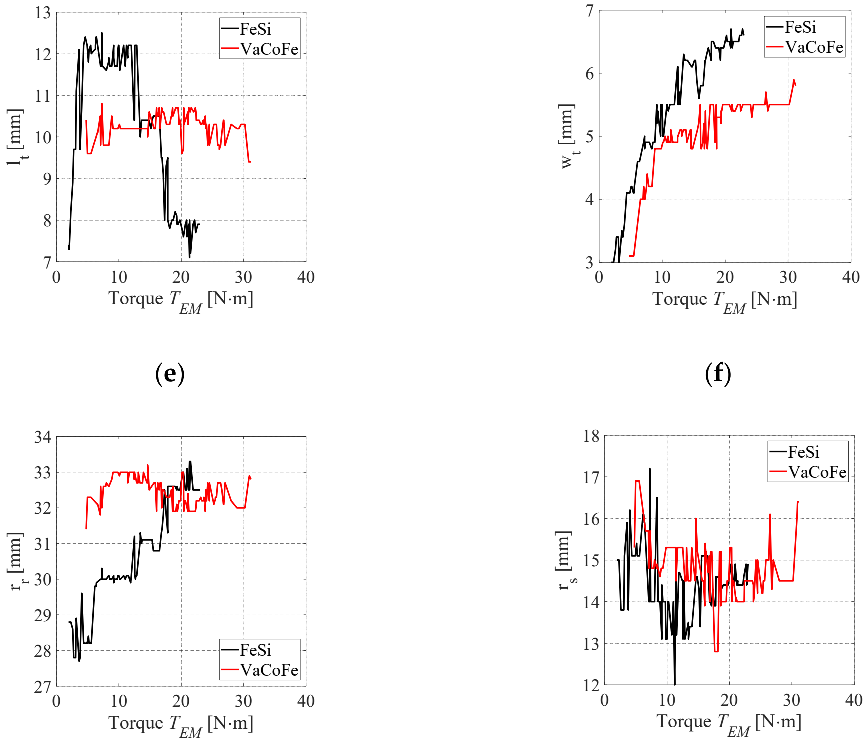

(e) (f)

(g) (h)

Figure 12. Decision variables for FeSi and VaCoFe core optimization sorted by increasing torque: a) stator outer ring width w, b) airgap size g, c) magnet length l_m, and d) width w_m, e) stator teeth length l_t and f) width w_t, g) rotor radius r_r and h) shaft radius r_s.

For both materials, permanent magnet dimensions are at the maximum possible without them overlapping to maximize linked flux and torque, Figure 12c) and d). The VaCoFe case allows wider magnets and, therefore, a higher magnetic flux.

The rotor and stator temperatures for the last generation, sorted by increasing torque, are presented in Figure 13. Because the cooling system is well-dimensioned, thermal constraints limit only the machine's upper performance limit, and torque increases mainly with the current density, Figure 11a). The magnetic constraint is the limiting factor as the magnetic flux density on both solutions is at the maximum value set, Figure 14. As such, as current density increases to maximize torque, efficiency decreases, and machine dimensions vary to keep the magnetic flux density around constraint level. This results in increased core volume with torque for FeSi, while for VaCoFe, core volume stays approximately constant from 20 N.m upwards, Figure 15a). The latter is possible because of the slight decrease in magnet size, compensated with the current density to achieve these higher torque values. It is estimated that, for machines with the same torque, the volume of VaCoFe core is, on average, 8.6 % less than that of FeSi one. However, because the density of VaCoFe (8120 kg/m^3) is higher than FeSi (7650 kg/m^3), the difference in core weight is less pronounced at 3.7 %, Figure 15b). Taking into account the weight of copper coils, PMs and a stainless-steel shaft, VaCoFe machines reach a maximum torque density of 7.2 N.m/kg and FeSi machines 5.4 N.m/kg. As such, it is possible to achieve higher torque densities with higher nominal torque points with VaCoFe.

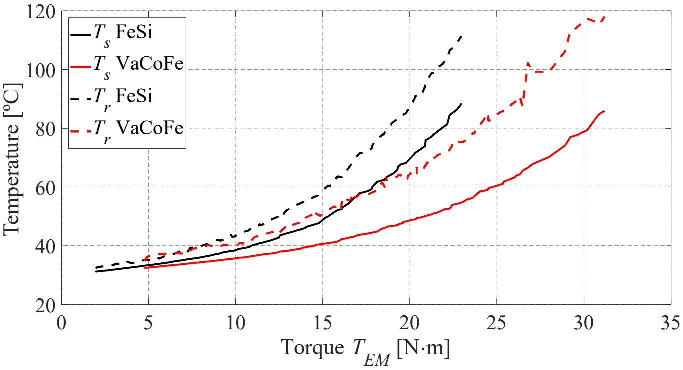

Figure 13. Surface and rotor temperatures of the last generation for FeSi and VaCoFe cores.

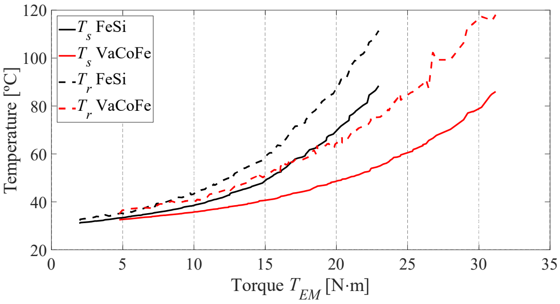

Figure 14. Maximum magnetic flux density of the last generation for FeSi and VaCoFe cores.

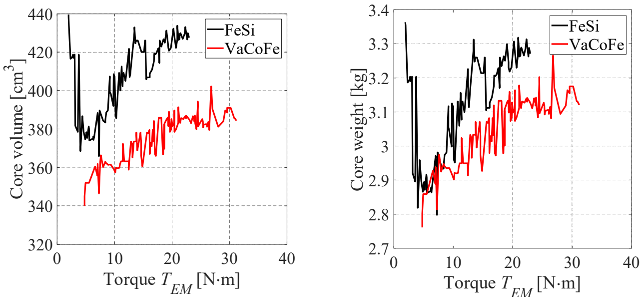

(**a**) (**b**)

Figure 15. Core a) volume and b) weight of the last generation for FeSi and VaCoFe cores.

For the competition vehicle application, specific torque is the most critical factor. The required nominal torque is 20 N.m per motor, so there is a potential 3.6 % increase in efficiency. The lower copper and PM weight makes up for the heavier core, however, both designs weigh around 4.3 kg. Additionally, for the same available space, VaCoFe allows reaching up to around 30 N.m, while the FeSi only to 23 N.m with lower levels of efficiency. Further analysis is needed on the impact of this on battery size and overall track performance to determine if the additional costs of manufacturing VaCoFe core motors are justified. These costs can be significant as the FeSi material for the prototype built in [11] was acquired at 237.4 €/kg while the VaCoFe laminations for the test circuit cost 770.7 €/kg (3.3 times higher cost than FeSi) and needs additional heat treatment to achieve optimum magnetic properties.

6. Detailed analysis of selected geometries

Three geometries are selected for further detailed analysis and validation of the optimization results: FeSi at 20 N.m (F20), VaCoFe at 20 N.m (V20) and 30 N.m (V30), corresponding to the Pareto front points presented in Figure 11b. These geometries are simulated with a rotating time-dependent 2D finite element model to obtain torque ripple and consider the effect of temporal and spatial flux density harmonics on core losses and overall efficiency. The selected optimized geometries are presented in Figure 16, and their dimensions in Table **3**.

It is noted that tooth lips were added to the stator teeth to consider a more realistic design than the simplified geometry considered for optimization. Between F20 and V20 the differences are mainly in the stator. The width of the magnetic circuit in F20 is wider to avoid core saturation as FeSi presents a lower saturation point than VaCoFe. V20 and V30 have similar dimensions with the slot current density being the main difference. Current density is the main factor in increasing torque as the temperature is not a limitation at this point, whereas core dimensions are defined by the saturation constraint.

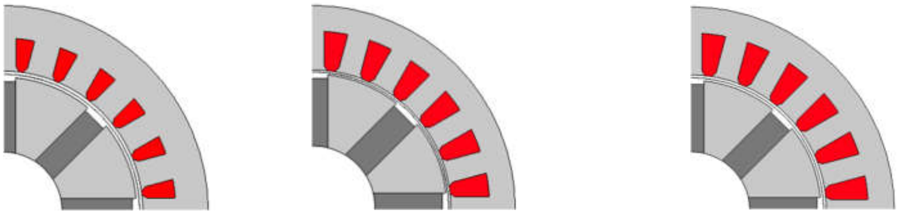

(**a**) (**b**) (**c**)

Figure 16. Selected optimized geometries: a) F20, b) V20, c) V30.

Table 3. Decision variables of selected geometries.

Variable	**F20**	**V20**	**V30**
r_r	32.5 mm	33 mm	32 mm
w_s	7.9 mm	6.3 mm	6.4 mm
w_m	6.2 mm	7.3 mm	6.5 mm
l_m	17.0 mm	16.6 mm	16.5 mm
w_t	6.4 mm	5.5 mm	5.5 mm
l_t	8.0 mm	9.6 mm	10.3 mm
g	1.5 mm	1.0 mm	1.3 mm
r_s	14.4 mm	15.3 mm	14.5 mm
J_{oq}	48.2 A/mm²	25.5 A/mm²	42.0 A/mm²
P_{PM}	17.57 W	18.66 W	39.27 W
P_{core}	65.1 W	62.41 W	64.66 W
P_{Cu}	875.5 W	391.4 W	1110 W
Efficiency	92.8 %	96.4 %	93.9 %
Torque density	4.7 N.m/kg	4.7 N.m/kg	7.1 N.m/kg

6.1. Core losses

Because the airgap is not constant, discrete winding distribution and voltage/current time harmonics, the magnetic flux density waveform is not purely sinusoidal. Also, in electrical machines, the magnetic fields are rotating, causing additional losses. To consider some of these effects, equation (5) is adapted by assuming that the total core loss is the sum of losses for each harmonic.

A FEM time-dependent simulation is used to obtain magnetic flux waveforms in the machine. The average magnetic flux density in each element is estimated considering the model's shape functions. Core losses in each element are computed by summing the separate contribution of the harmonics of the radial and tangential components of the magnetic flux density, obtained from Fourier transformation (21) [20].

$$p_i = \sum_n k_h f_n \left({B_r}_{n,i}^2 + {B_\theta}_{n,i}^2 \right) + k_e f_n^2 \left({B_r}_{n,i}^2 + {B_\theta}_{n,i}^2 \right) + k_{exc} f_n^{1.5} \left({B_r}_{n,i}^{1.5} + {B_\theta}_{n,i}^{1.5} \right) \tag{21}$$

In (21), p_i is the core loss density in element i, f_n is the nth frequency harmonic and B_r and B_θ are the radial and tangential magnetic flux density components respectively. k_h, k_e

and k_{exc} are the hysteresis, eddy current, and excess losses coefficients, obtained from the material's specific losses curve. The steps to compute p_i for a specific element i are presented in Figure 17. The exemplified element is located near the tip of the stator tooth, Figure 17a). The magnetic flux density here is non-sinusoidal and presents a high tangential component as it is affected by the variation of reluctance from the non-uniform airgap during rotation, Figure 17b). As such, there is a relevant harmonic content that, from (21), contributes to higher core loss density in elements near the airgap than in other parts of the machine where the flux density waveform is more sinusoidal.

Because the flux distribution is computed from the 2D simulation it is assumed that the flux distribution is the same along the length, L, of the machine. Total core losses, P_{core}, are obtained from the sum of the losses in each element, i, density ρ and area A_i, (22).

$$P_{core} = \sum_i \rho A_i L \cdot p_i \tag{22}$$

In conductive materials with induced currents, such as permanent magnets and shaft, Joule losses are computed from (23), where V is the PMs volume, σ the conductivity and $\mathbf{J}$ the PMs induced current density variation in time.

$$P_{PM} = \int_V \frac{|\mathbf{J}|^2}{\sigma} dV \tag{23}$$

The efficiency is computed considering winding losses, as in the previous section, and core and induced current losses with these presented methods.

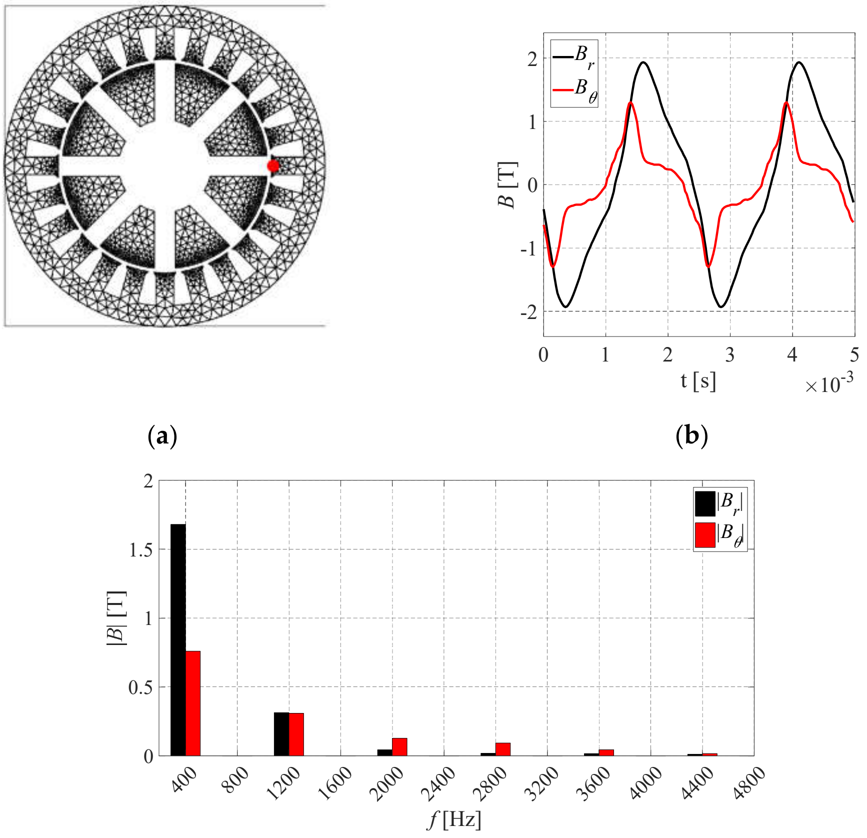

(**a**) (**b**)

(**c**)

Figure 17. Steps for computation of losses density, example for element i. a) Example of core geometry mesh, b) waveform of flux density radial and tangential components in element i, c) waveforms' Fourier transformation.

6.2. Results

The selected geometries are simulated with a 2D time-dependent simulation for the optimized load angle (i_d=0 and i_q=I_m) at nominal electrical frequency 400Hz. The magnetic flux density distribution is, as expected, with the flux density norm in the stator teeth around the set maximum for optimization (1.6T for FeSi and 2.2T), Figure 18. The slight differences between optimization results and simulation are due to the changes made to the simplified geometry.

The instantaneous torque in time is presented in Figure 19 for the selected geometries. The spoke-type IPMSM results in a relatively higher torque ripple than other topologies due to the flux concentration in the airgap [24]. VaCoFe's higher saturation point allows higher flux concentration in the airgap and, consequently, V20 and V30 present higher torque ripple than F20. V20 presents a peak-to-peak ripple of 7 N.m, V30 of 5.6 N.m and F20 of 2.1 N.m. However, the ripple could be reduced while approximately maintaining the average torque with further analysis focused on dimensioning a non-uniform airgap that distributes the flux in the airgap more evenly, through shaping the rotor poles and/or stator teeth [24]. Preliminary results of these adjustments are shown further.

The average torque values predicted with the 2D stationary (2D static) model used for optimization, based on stationary simulations, are in accordance with the results obtained from the 2D time-dependent (2D-time) simulation with a maximum deviation of 2.28 % for the V20 geometry, as presented in Table 4. This low deviation is mainly due to the parameterization of the *d-q* model with 2D FE simulation which considers the non-linearity of the magnetic circuit and saturation of the material. Nonetheless, the model does not consider ripple and harmonics, so some deviations are expected.

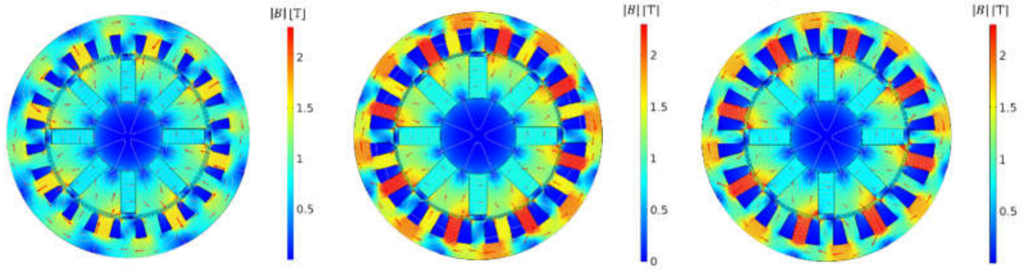

(**a**) (**b**) (**c**)

Figure 18. Distribution of magnetic flux distribution of selected geometries a) F20, b) V20 and c) V30.

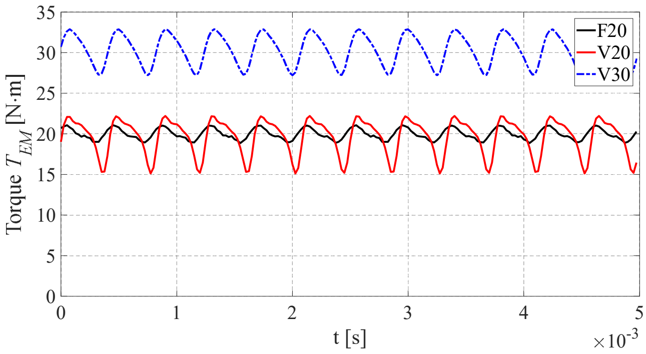

Figure 19. Instantaneous torque considering i_d=0 of selected geometries: F20, V20 and V30.

Table 4. Average torque and efficiency obtained from 2D stationary model and 2D time-dependent model.

	Avg. Torque [N.m]		**Efficiency [%]**	
	2D-time	**2D-static**	**2D-time**	**2D-static**
F20	19.95	19.78 (-0.84%)	93.11	92.84 (-0.27%)

V20	19.62	20.07 (+2.28%)	96.31	96.39 (+0.08%)
V30	30.31	29.81 (-1.64%)	94.21	93.92 (-0.29%)

In terms of efficiency, there is a maximum difference of 0.29 % for the V30 geometry. The accuracy of the efficiency depends mostly on the estimation of losses, as output power is similar. Figure 20 presents the separation of the losses computed with time-dependent FE simulation and the stationary model used on optimization based on stationary FE simulations for the chosen geometries. Because copper losses account for most of the total losses of the motor and these are computed the same way in both models, both give similar values of efficiency. It is noted that the skin effect can cause additional losses limiting the maximum slot windings' wire gauge to a 2.8mm radius (skin depth at 533Hz/8000rpm). This is achieved with multi-strand wires with a thickness less than 1mm, with multiple conductors in parallel as done in the previous FeSi IPMSM [11]. Despite the simplifications made for the computation of permanent magnet and core losses, considering only the magnetic flux's fundamental component done in the optimization model, results seem to be a close overestimation of the ones obtained using the FE time-dependent model. For both models, the iron losses give similar results, with slightly higher values obtained with time-dependent FE simulation, because of the additional effects considered computing them. The overestimation is due to differences in the estimation of losses in the permanent magnet and shaft. This is because in the optimization model the whole magnet volume is considered to be affected by the same magnetic flux variation. On the other hand, with time-dependent FE simulation, the non-uniform distribution of induced currents is captured, and losses are produced only in regions closer to the airgap.

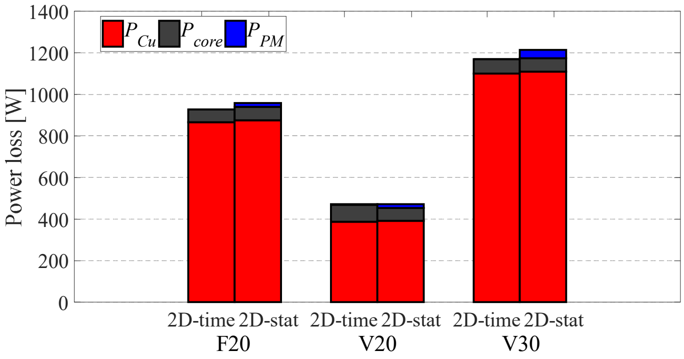

Figure 20. Losses computed using 2D time-dependent FE simulation (2D-time) and the 2D stationary model used for optimization (2D-static) for the chosen geometries.

In addition, the higher torque ripple of the V20 and V30 topologies could also be reduced with changes to the shape of the rotor by, for example, adding protrusions around the magnets as seen in Figure 21. This results in a more even flux distribution in the airgap, reducing ripple and approximately maintaining the average torque. Using this geometry, V20 and V30 present similar average torque 20.78 N.m and 29.92 N.m, respectively. The peak-peak torque ripple is reduced from 7.0 N.m to 4.3 N.m for the new V20 and from 5.6 N.m to 4.6 N.m for the new V30, Table 5. These results were obtained using a 2D-time dependent simulation. Additional torque ripple attenuation could be achieved by also adjusting the curvature shape of the rotor poles or the stator tooth lips, which will be further analyzed, for the final construction of the prototypes.

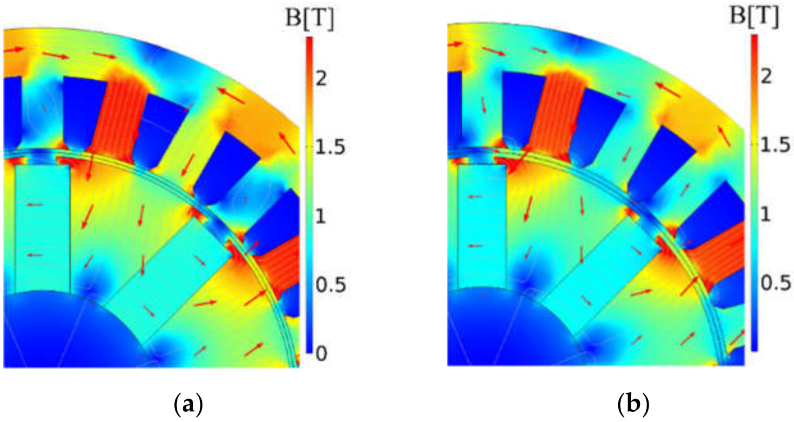

(**a**) (**b**)

Figure 21. Magnetic flux distribution of geometries with changed rotor shape of (a) V20 - new and (b) V30 - new.

The flux density distribution in the permanent magnets was also analyzed at maximum torque and maximum direct current (i_d=I_m) conditions. For the three presented geometries the simulation does not suggest considerable demagnetization, with flux density levels above the knee-point (0.4T for the N40H magnets at worst-case 120ºC), in most of the magnets, for both cases. At the nominal operating point, because the machine geometries are optimized for maximum torque at id=0, the resulting power factor is high for all geometries being 0.990 for F20, 0.994 for V20 and 0.980 for V30.

Table 5. Average torque and Torque ripple.

Geometry	Avg. Torque [Nm]	Peak-peak Torque ripple [Nm]
V20	19.62	7.0
V20 - new	20.78	4.3
V30	30.31	5.6
V30 -new	29.92	4.6

7. Conclusions

A spoke-type IPMSM geometry is optimized considering FeSi and VaCoFe cores for a range of torque/efficiency to provide a general comparative analysis between materials. This is particularized for a 4-motor competition vehicle's powertrain. A genetic optimization algorithm (NSGA-II) is applied over a hybrid analytical/finite-element model of the motor to provide sufficiently accurate electromagnetic and thermal results within a feasible time. The characterization of the materials for the optimization model is based on each's magnetic properties, in particular, VaCoFe *B-H* curve was obtained experimentally and presented.

According to the presented model, it is shown that VaCoFe core results in a better machine across both torque and efficiency ranges. VaCoFe can result in an estimated increase of up to 5 % in efficiency for the same torque, or up to 64 % torque increase for the same efficiency level. For the same available space, the VaCoFe can reach up to around 30 N.m, while the FeSi only 23 N.m with lower levels of efficiency.

These results are dependent on the accuracy of the presented 2D-static model, where only the magnetic flux's fundamental component is considered in computation of permanent magnet and core losses. Also, because VaCoFe can cost around 3.3 times more than FeSi, more than usual attention to simulation accuracy is necessary before investing and building a final prototype. A more accurate time-dependent 2D simulation was used to evaluate three chosen geometry designs and a method was implemented to compute discriminated losses in the windings, PMs and core material. Two geometries of VaCoFe and FeSi with 20 N.m, the target torque of the in-wheel motors for the competition vehicle, and a VaCoFe at 30 N.m, around the maximum torque motor obtained through optimization, were analyzed.

It is shown that the analytical/finite-element model used for optimization, based on stationary simulations of a quarter of the machine's magnetic circuit, gives results in accordance with the commonly more accurate time-dependent simulation, with deviations lower than 2.28 % for the average torque and 0.29 % in efficiency, with less computational cost, for the studied operation point. As such it might be used for similarly computation intensive studies, as a first approach, to machine design as a quicker and almost as accurate alternative to FE model-based approaches.

Comparing the selected geometries, the torque ripple is higher for the VaCoFe designs than the FeSi one, mainly because of the higher flux density in the airgap. However, this can be attenuated through adjusting the shape of the rotor poles through further optimizations of the obtained designs with this objective. Overall, further analysis is needed using a more complete 3D model for the machine to study additional effects, (e.g. border effects), not accounted for in 2D models.

The presented analysis is promising towards building final prototypes and provides a comparative analysis of the possible advantages in using VaCoFe as an alternative core material to traditional FeSi for high specific-torque electric vehicles and aircrafts applications. The authors are now working in the construction of the optimized geometry of the VaCoFe machine.

Author Contributions: Conceptualization, methodology, PPCB and JFPF; validation, PPCB and JFPF; formal analysis, investigation, PPCB; resources, JFPF and PJCB; writing—original draft preparation, writing—review and editing, PPCB, LFDB, JFPF and PJCB; supervision, JFPF and PJCB. All authors have read and agreed to the published version of the manuscript.

Acknowledgments: This work is financed by national funds through FCT - Foundation for Science and Technology, I.P., through IDMEC, under LAETA, project UIDB/50022/2020.

Conflicts of Interest: Declare conflicts of interest or state "The authors declare no conflict of interest." Authors must identify and declare any personal circumstances or interest that may be perceived as inappropriately influencing the representation or interpretation of reported research results. Any role of the funders in the design of the study; in the collection, analyses or interpretation of data; in the writing of the manuscript, or in the decision to publish the results must be declared in this section. If there is no role, please state "The funders had no role in the design of the study; in the collection, analyses, or interpretation of data; in the writing of the manuscript, or in the decision to publish the results".

References

1 NASA Aeronautics; NASA Aeronautics Strategic Implementation Plan: 2019 Update. *Technical Report NP-2017-01-2352-HQ; National Aeronautics and Space Administration* (NASA): Washington, DC, USA, 2019.

2 Jayaraman, T.; Effect of Processing of HIPERCO® 50 Alloy Laminates on Their Magnetic Properties. *Journal of Electronic Materials*, 2025, vol. 44, p. 4379–4386.

3 Krings, A. ; Cossale, M. ; Tenconi, A.; Soulard, J.; Cavagnino, A.; and Boglietti, A.; Magnetic materials used in electrical machines: a comparison and selection guide for early machine design. *IEEE Industry Applications Magazine*, 2017, vol. 23, no. 6, pp. 21-28.

4 Zhang, X; Haran, K. S.; High-specific-power electric machines for electrified transportation applications-technology options. *2016 IEEE Energy Conversion Congress and Exposition (ECCE)*, Milwaukee, WI, 2016.

5 Palmieri, M.; Perta, M.; Cupertino, F.; Design of a 50.000-r/min Synchronous Reluctance Machine for an Aeronautic Diesel Engine Compressor. *IEEE Transactions on Industry Applications*, 2016, vol. 52, no. 5, pp. 3831-3838.

6 Fernando, N.; Vakil, G.; Arumugam, P.; Amankwah, E.; Gerada, C.; and Bozhko, S.; Impact of Soft Magnetic Material on Design of High-Speed Permanent-Magnet Machines. *IEEE Transactions on Industrial Electronics*, 2017, vol. 64, no. 3, pp. 2415-2423.

7 Mecrow, B. C. e. al;. Design and testing of a four-phase fault-tolerant permanent-magnet machine for an engine fuel pump. *IEEE Transactions on Energy Conversion*, 2004, vol. 19, no. 4, pp. 671-678.

8 Krings, A.; Boglietti, A.; Cavagnino, A.; and Sprague, S.; Soft Magnetic Material Status and Trends in Electric Machines," *IEEE Transactions on Industrial Electronics*, 2017, vol. 64, no. 3, pp. 2405-2414.

9 Volbers, N.; and Gerster, J.; High Saturation, High Strength Iron-Cobalt Alloy for Electrical Machines. *INDUCTICA, CWIEME*, 2012.

---

10 Zhang, X.; Bowman, C. L.; O'Connell, T.; Haran, K. S.; Large electric machines for aircraft electric propulsion. *IET Electric Power Applications*, 2018, vol. 12, pp. 767-779.

11 Bhagubai, P.; Sarrico, J.; Fernandes, J.; Branco, P.; Design, Multi-Objective Optimization, and Prototyping of a 20 kW 8000 rpm Permanent Magnet Synchronous Motor for a Competition Electric Vehicle. *Energies*, 2020, vol. 13, no. 10, p. 2465.

12 Deb, K.; Pratap, A.; Agarwal, S.; and Meyarivan, T.; A Fast Elitist Multiobjective Genetic Algorithm NSGA-II. Evol. Comput., 2002, vol. 6, p. 182–197.

13 Han, W. ; van Dang, C.; Kim, J.; Kim, Y.; and Jung, S.; Global-Simplex Optimization Algorithm Applied to FEM-Based Optimal Design of Electric Machine. *IEEE Trans. Magn*, 2017, vol. 53, p. 1–4.

14 Bianchi, N.; and Bolognani, S. D.; Optimisation of Electric Motors by Genetic Algorithms. *IEE Proc. Electr. Power Appl.*, 1998.

15 Fatemi, A.; Ionel, D. M.; Popescu, M.; Chong, Y. C.; and Demerdash, N. A. O.; Design Optimization of a High Torque Density Spoke-Type PM Motor for a Formula E Race Drive Cycle. *IEEE Transactions on Industry Applications*, 2018, vol. 54, no. 5, pp. 4343-4354.

16 Kesgin, M. G.; Han, P.; Taran, N.; and Ionel, D. M.; Optimal Study of a High Specific Torque Vernier-type Axial-flux PM Machine with Two Different Stators and a Single Winding. *2020 IEEE Energy Conversion Congress and Exposition (ECCE)*, 2020.

17 Fatemi, A.; Ionel, D. M.; Demerdash, N. A. O.; and Nehl, T. W.; Optimal Design of IPM Motors With Different Cooling Systems and Winding Configurations. *IEEE Transactions on Industry Applications*, 2016, vol. 52, no. 4, pp. 3041-3049.

18 Bhagubai, P. P. C. ; Cardoso, A. C.; and Fernandes, J. F. P.; Cobalt Iron Core Impact on Optimal Design of an Interior Permanent Magnet Synchronous Motor for Competition Electric Vehicle. *2020 2nd Global Power, Energy and Communication Conference (GPECOM)*, Izmir, Turkey, 2020.

19 Lee, J.-Y. ; Lee, S.-H.; Lee, G.-H.; Hong, J.-P.; and Hur, J.; Determination of Parameters Considering Magnetic Nonlinearity in an Interior Permanent Magnet Synchronous Motor. *IEEE Trans. Magn*, 2006, vol. 42, p. 1303–1306.

20 Yamazaki K.; Seto, Y.; Iron loss analysis of interior permanent-magnet synchronous motors-variation of main loss factors due to driving condition. *IEEE Transactions on Industry Applications*, 2006, vol. 42, no. 4, pp. 1045-1052.

21 Yamazaki, K.; Fukuoka, T.; Akatsu, K.; Nakao, N.; and Ruderman, A.; Investigation of Locked Rotor Test for Estimation of Magnet PWM Carrier Eddy Current Loss in Synchronous Machines. *IEEE Trans. on Magn.*, 2012, vol. 48, p. 3327–3330.

22 Huang, W.; Bettayeb, A.; Kaczmarek, R.; and Vannier, J.; Optimization of Magnet Segmentation for Reduction of Eddy-Current Losses in Permanent Magnet Synchronous Machine. *IEEE Trans. Energy Convers.*, 2010, vol. 25, p. 381–387.

23 Fénot, M.; Bertin, Y.; Dorignac, E.; and Lalizel, G.; A Review of Heat Transfer between Concentric Rotating Cylinders with or without Axial Flow. *Int. J. Therm. Sci.*, 2011, vol. 50, p. 1138–115.

24 Hwang, K. Y. ; Jo, J. H.; and Kwon, B. I.; A Study on Optimal Pole Design of Spoke-Type IPMSM With Concentrated Winding for Reducing the Torque Ripple by Experiment Design Method. *IEEE Transactions on Magnetics*, 2009, vol. 45, no. 10, pp. 4712-4715.

25 Kuptsov, V.; Fajri, P.; Trzynadlowski, A.; Zhang, G.; and Magdaleno-Adame, S.; Electromagnetic Analysis and Design Methodology for Permanent Magnet Motors Using Motor Analysis-PM Software. *Machines*, 2019, vol. 7, p. 75.